Subgrid-scale backscatter in a supersonic combusting shear layer with an oblique shock

By C. M. Helm†‡, D. Brouzet, B. Bornhoft, T. P. Gallagher¶,
AND D. M. Peterson‡

Spatially developing compressible shear layers, both reacting and nonreacting, are numerically simulated in order to study the turbulent kinetic energy (TKE) cascade in a reacting shear layer. In supersonic shear layers, shock waves and expansion fans can interact with both the compressible turbulence and the flame front. Here we consider the configuration of a spatially developing shear layer interacting with an oblique shock. This paper documents the high-fidelity numerical simulations of the configuration of interest, as well as initial statistics of the TKE backscatter calculated at various filter scales.

1. Introduction

Compressible combustion flow fields typical of high-speed propulsion systems exhibit a rich set of dynamics involving the flame, the turbulence, and the compressible behavior of the overall flow field. Thin shocks and flame structures combined with high Reynolds numbers make numerically resolving such flows at engineering-relevant conditions impractical due to the excessive numerical resources required. The development of reliable and accurate modeling approaches is therefore necessary. A traditional view of low-Mach-number, nonreacting turbulence is the energy cascade of Richardson (1922), which describes the turbulent kinetic energy as being generated at the largest scales of motion and then transferred inviscidly to smaller and smaller scales until the energy is dissipated into heat at the smallest (viscous) length scales (Pope 2000; Tennekes & Lumley 1972). The drain of energy at the smallest, subgrid scales (SGS) is the classic assumption used in the eddy-viscosity-type closure models for large eddy simulation (Smagorinsky 1963). The validity of the net-downward energy cascade assumption for high-speed reacting turbulence is an open research question.

Compressibility due to high Mach number, amplification of turbulence by shock waves, and deposition of chemical energy at very small scales associated with the flame length scale all have the potential to alter the behavior of the energy transfer process. The transfer of energy across scales can be studied by considering the budget of TKE and specifically the backscatter term that appears in this equation (Piomelli *et al.* 1991). Kazbecov & Steinberg (2021) studied the cross-scale TKE transfer in swirl burner premixed flames and found that, for their nonreacting experiments, there is a net transfer of TKE across the filter width into the small scales. However, in the reacting cases, a positive net backscatter of TKE from subgrid to large scales was observed near the flame brush. The same authors (Kazbecov & Steinberg 2022) also demonstrated that large-scale coherent vortical structures in the reacting shear layer had a direct effect on

† Innovative Scientific Solutions Inc.
‡ Air Force Research Laboratory, Wright-Patterson Air Force Base
¶ Air Force Research Laboratory, Edwards Air Force Base

the local variation of backscatter strength. O'Brien *et al.* (2014b, 2017) similarly showed that net TKE backscatter occurs in the flame brush of a subsonic, premixed laminar flame in isotropic turbulence. A correlation between backscatter and pressure-dilatation was found to be directly related to the flow expansion from chemical heat release of the flame. O'Brien *et al.* (2014a) studied a nonpremixed, supersonic temporal mixing layer. In this supersonic mixing layer, they did not find any net backscatter, but they found a correlation between instantaneous TKE backscatter and pressure-dilation work caused by compressibility effects.

The purpose of the current project is to investigate to what extent the turbulence energy cascade process is altered by strong compressibility effects in reacting turbulence at conditions relevant to high-speed hydrocarbon-fueled propulsion systems. The intended outcome of this research is to provide physical insights into the energy cascade processes at these conditions in order to determine to what extent the current models are insufficient and what physical mechanism need to be accounted for by the models for them to be more accurate and predictive. In this work we consider the behavior of the cross-scale TKE backscatter in the numerical simulations of a spatially developing shear layer interacting with an impinging oblique shock. Both reacting and nonreacting shear layers are considered. The spatial configuration allows for the proper convergence of the time-averaged statistics due to the stationary nature of the flow as opposed to the more common temporally developing shear layer studies. It also allows for the study of the interaction between the shear layer and an oblique shock. Additionally, our simulations use ethylene as the fuel, as opposed to previous research efforts (O'Brien *et al.* 2014a, 2014b) that have considered dilute hydrogen, which has shorter chemical timescales and lower heat release due to the dilution.

2. Computational method

The cell-centered finite-volume solver US3D (Nompelis *et al.* 2004) is used to solve the reacting, compressible Navier-Stokes equations for all simulations performed here. Ethylene combustion is modeled using the 22-species, 206-step reduced mechanism of Luo *et al.* (2012), which is able to accurately reproduce the ignition delay, laminar flame speed, and extinction strain rate of the detailed mechanism from which it was derived. The numerical method is such that the central portion of the flux is fourth-order accurate for linear problems on Cartesian grids. The upwind flux used is the modified Steger-Warming flux vector splitting scheme of MacCormack & Candler (1989). A compressibility-based shock detection switch is used to apply the upwind scheme only near discontinuities, as discussed by Hassan *et al.* (2016). The time integration scheme is the explicit third-order accurate total-variation diminishing Runge-Kutta scheme of Gottlieb & Shu (1998).

2.1. *Pantano & Sarkar case*

Following O'Brien *et al.* (2014a), the current simulation approach is validated against the temporal shear layer DNS data of Pantano & Sarkar (2002) (P&S). The case considered here is a nonreacting temporally evolving shear layer with a convection Mach number of 0.7. The convective Mach number is defined as $M_c = \Delta u/(c_1 + c_2)$, where Δu is the velocity difference across the shear layer, and c_1 and c_2 are the speed of sound for the top and bottom streams respectively. The density ratio s across the shear layer for this case is unity. The initial Reynolds number is 160, where Reynolds number is defined as $Re_\theta^0 = \Delta u \delta_\theta{}^0/\nu_1$ based on the velocity difference, the top stream kinematic viscosity ν_1,
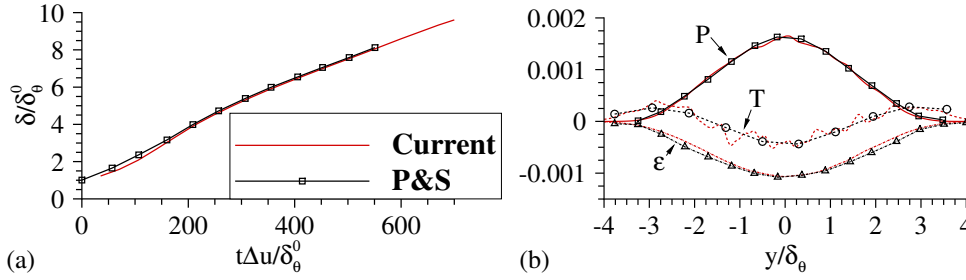
Figure 1: (a) Shear layer growth rate (b) and TKE budget terms for the DNS of P&S and for the current simulation approach. All TKE terms are normalized by $\Delta u^3/\delta_\theta$.

and the initial momentum thickness δ_θ°. The definition of the momentum thickness is given in Eq. (2.1), where the tilde indicates a Favre-averaged quantity such that $\tilde{\phi} = \overline{\rho\phi}/\bar{\rho}$,

$$\delta_\theta = \frac{1}{(1+s)} \int_{-\infty}^{+\infty} \frac{\bar{\rho}}{\rho_1} \left[1 - \left(\frac{2\tilde{u}}{\Delta u} \right)^2 \right] dy. \tag{2.1}$$

Simulations of the P&S $M_c = 0.7$ temporal shear layer were performed using the simulation method described above on a Cartesian grid of $256 \times 192 \times 128$ cells in the x, y and z directions, respectively. The size of the domain is $172 \times 129 \times 86$ in units of δ_θ°. The grid is periodic in the x and z directions and characteristic outflow boundaries are used at the boundaries in the y direction. The shear layer was initialized with a hyperbolic tangent mean streamwise velocity profile $u(y) = \Delta u/2 \tanh(-y/2\delta_\theta^\circ)$. The spanwise and cross-stream velocity components were set to zero. In order to facilitate breakdown of the shear layer into turbulence, velocity fluctuations were added to the mean velocity profile. These fluctuations were generated using a digital filtering approach based on the work of Touber & Sandham (2009). The magnitude of the fluctuations was scaled so that the resulting nondimensional Reynolds stresses were consistent with the magnitudes found in the fully developed flow of P&S.

Figure 1(a) shows the time history of the shear layer momentum thickness δ_θ normalized by its initial value δ_θ°. Time is normalized by $\delta_\theta^\circ/\Delta u$. Initially, the current simulation approach shows a slightly slower growth rate for the shear layer in comparison to the P&S data which is likely due to the difference in initialization techniques used. By approximately 150 nondimensional timescales, however, the current simulation matches the results of P&S quite well showing a distinct linear growth region.

The current simulation approach is further evaluated by comparing the most significant terms from the TKE budget equation with those reported by P&S. TKE is defined as $K = R_{kk}/2$, where the Reynolds stress tensor is given by $R_{ij} = \overline{\rho u_i'' u_j''}/\bar{\rho}$. The overbar represents an average in the streamwise and spanwise periodic directions. The quantity u_i'' is the Favre fluctuation of velocity and ρ is the local density profile as a function of y. The budget terms plotted in Figure 1(b) are the production term $\mathcal{P} = \overline{u_i'' u_k'' \partial u_i''}/\partial x_k$, the dissipation term $\epsilon = \overline{\tau_{ik} \partial u_i''/\partial x_k}$, and the transport term $\mathcal{T} = 1/2 \, \partial \overline{\rho u_i'' u_i'' u_k''}/\partial x_k$. In the dissipation term, $\tau_{ij} = 2\mu(S_{ij} - S_{ii}\delta_{ij}/3)$ is the viscous stress tensor, where $S_{ij} = 1/2 \, (\partial u_i/\partial x_j + \partial u_j/\partial x_i)$, μ is the molecular viscosity, and δ_{ij} is the Kronecker delta. Figure 1(b) shows the budget terms from the DNS of P&S, which were averaged
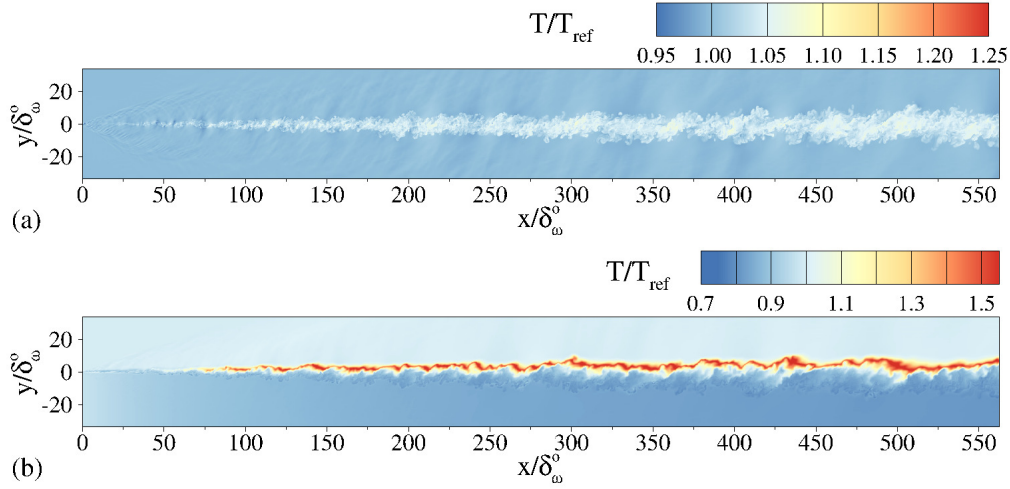
Figure 2: Instantaneous temperature of the (a) nonreacting and (b) reacting spatially developing mixing layers.

over the self-similar region of the time history by scaling the instantaneous results by the local momentum thickness. In order to converge the current results, 32 separate realizations using distinct initializations were averaged at a nondimensional time of 600. The comparison of the averaged budget terms shown in Figure 1(b) indicates that the current numerical approach produces results that are consistent with those of P&S. However, additional realizations or averaging appears to be required to provide a smoother curve for the transport term. The results provide confidence in the ability of our numerical approach to accurately produce the shear layer simulations to be described in the next section.

3. Problem description

In this section we present preliminary results of four separate simulations. The first two simulations are of canonical spatially developing mixing layers (SDML), one nonreacting with air in both streams and the other reacting with air in the top stream and pure ethylene in the bottom stream. These two simulations are referred to throughout this paper as SDML-NR and SDML-R. Both have a convective Mach number of 0.7 and a density ratio of unity so as to be consistent with the validation case of P&S in Section 2.1. For both simulations, the top stream is dry air at a temperature of 2000 K. The bottom air stream for the nonreacting case is also at 2000 K, while for the reacting case the bottom stream of ethylene is initially at a temperature of 1937 K. These conditions were selected on the basis of the simulations of a high-enthalpy supersonic combustion duct as discussed in Helm *et al.* (2025). The lower temperature of the ethylene was required to maintain the density ratio of 1. These temperatures are high enough that the shear layer will auto-ignite. The pressure for the current simulations was set to 20 kPa to be consistent with the regions of peak pressure in the combustion duct simulations.

The flow is initialized similar to the P&S case above, with time-varying fluctuations added to the inflow. All simulations presented here are periodic in the spanwise direction. Characteristic subsonic boundaries are used on the top and bottom, and extrapolation
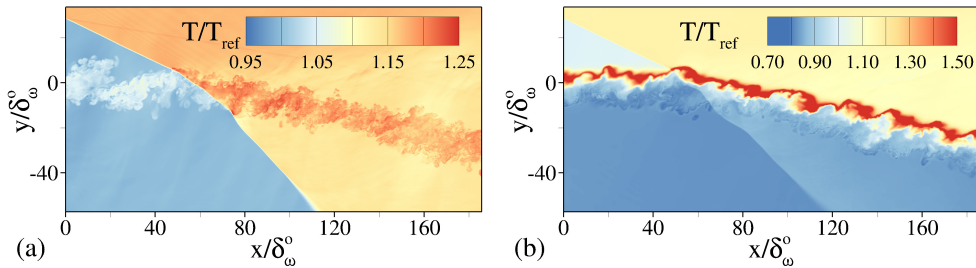
Figure 3: Instantaneous temperature of the shocked (a) nonreacting and (b) reacting shear layers.

is used on the outflow. Both the nonreacting and reacting shear layers use the same grid of size $3584 \times 272 \times 128$ cells with outer dimensions of $560 \times 270 \times 20$ in units of the vorticity thickness of the assigned inflow profile $\delta_\omega{}^\circ = 1.6$ mm. The grid spacing is uniform in all three spatial directions for $y/\delta_\omega{}^\circ$ within ± 15, beyond which the y direction grid is stretched. Figure 2 shows an instantaneous realization of the temperature at the center xy plane for the SDML-NR (panel a) and the SDML-NR (panel b). Temperature is nondimensionalized by $T_{\text{ref}} = 2000$ K. Mean flow conditions including the Mach number and temperature of the two streams as well as the vorticity and momentum thickness are provided in Table 1. All quantities reported in Table 1 and all mean flow statistics for the SMDL-NR and SDML-R have been evaluated from statistics collected by averaging in time, over the spanwise direction, and over a streamwise range $470 < x/\delta_\omega{}^\circ < 530$. Over this distance, the change in momentum thickness is less than 10%, so no scaling of the y axis was done for the streamwise averaging. Also included in Table 1 are the Reynolds numbers, calculated using the viscosity of the air, and the interior grid spacing h, normalized by the local momentum thickness.

The second set of two simulations includes the shocked shear layers at both the nonreacting and reacting conditions, referred to as SDML-NR-Shocked and SDML-R-Shocked, respectively. These were run by collecting the flow statistics at a streamwise station at $x/\delta_\omega{}^\circ = 375$ in the previous two runs and then interpolating them onto the inflow boundary of the shocked simulations. The shock is introduced at the inflow boundary by enforcing the Rankine-Hugoniot jump condition for an oblique shock at a $26°$ angle to the freestream. This was chosen to create a pressure jump of a factor of two across the shock on the air side. Figure 3 shows the instantaneous temperature contours for the two shocked shear layers. Both simulations use the same grid of $1200 \times 543 \times 128$ cells with outer dimensions of $(190 \times 270 \times 20)\delta_\omega{}^\circ$. The grid spacing is uniform throughout for $-41 < y/\delta_\omega{}^\circ < 31$, beyond which the y grid is stretched. In order to have an oblique shock pass entirely through the shear layer, both streams need to be supersonic. With a lower stream Mach number of about 1.9, supersonic flow could be maintained in the shear layer with both combustion and an oblique shock. With the lower Mach number set, an upper stream Mach number of 3.1 is needed to produce a convective Mach number of 0.7.

In Table 1, the free-stream Mach numbers and temperatures listed for the shocked cases are the postshock conditions. Mean statistics for the postshock shear layer are calculated by rotating the grid coordinates and velocity field by $13°$ so that they are parallel to the deflected shear layer, and then taking averages in time, in the spanwise

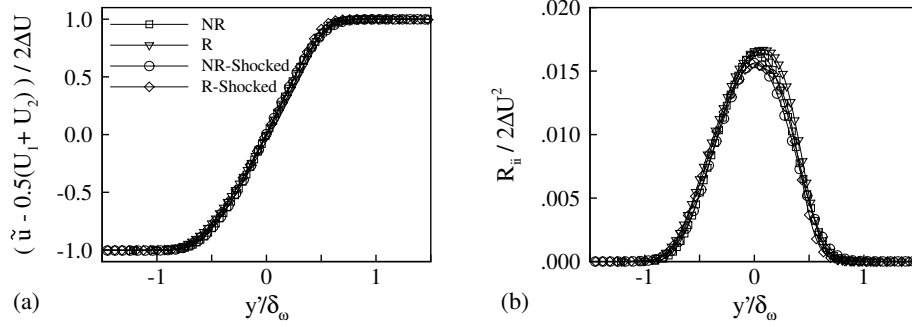| Case	M_c	M_1	M_2	$T_1[\mathrm{K}]$	$T_2[\mathrm{K}]$	$\delta_\theta[\mathrm{mm}]$	$\delta_\omega[\mathrm{mm}]$	Re_θ	Re_ω	h/δ_θ
SDML-NR	0.71	3.1	1.7	2000	2000	5.4	28.8	3730	19,740	0.046
SDML-R	0.77	3.1	2.0	2000	1630	4.6	27.8	3130	19,110	0.055
SDML-NR-Shocked	0.72	2.8	1.3	2280	2270	4.2	22.1	4400	23,160	0.050
SDML-R-Shocked	0.79	2.8	1.7	2260	1670	3.9	23.5	3870	23,650	0.065

Table 1: Shear layer stream conditions.

Figure 4: Cross-layer mean profiles of normalized (a) streamwise velocity and (b) TKE.

direction, and over a streamwise range that, in the nonrotated coordinates, crosses the shear layer center within $145 < x/\delta_\omega{}^\circ < 180$.

Mean profiles in Figure 4 show that neither the oblique shock nor the flame has a significant effect on the mean velocity or the TKE of the shear layer. Both profiles in Figure 4 are normalized using the velocity difference across the layer ΔU. The y' axis is the coordinate direction that is locally perpendicular to the center line of the shear layer positioned so that $y' = 0$ is the point at which the velocity is equal to the average of the two streams. The cross-stream coordinate y' is normalized by the local vorticity thickness. Figure 4(a) shows no significant distortion of the velocity profile in either the reacting or the shocked data, while Figure 4(b) indicates that the shock does not significantly enhance the mean TKE. The TKE is only slightly reduced on the flame side (positive y') for the reacting cases.

4. Analysis

In this section we present initial *a priori* calculations of the TKE backscatter in the SDML data of Section 3. The equation for the budget of resolved TKE, $k = \tilde{u}_i \tilde{u}_j / 2$, can be written as

$$\frac{\partial \bar{\rho} k}{\partial t} + \frac{\partial \bar{\rho} \tilde{u}_i k}{\partial x_i} = \frac{\partial \bar{\tau}_{ij} \tilde{u}_j}{\partial x_i} - \frac{\partial \mathcal{T}_{ij} \tilde{u}_j}{\partial x_j} - \frac{\partial \bar{p} \tilde{u}_i}{\partial x_i} + \Pi - \epsilon_\nu - \epsilon_{SGS}. \tag{4.1}$$

On the left-hand side are the time rate of change of TKE and the convection term. The first three terms on the right-hand side are transport terms responsible for the redistribution of TKE. The remaining three terms on the right side are the pressure-dilatation work $\Pi = \bar{p}(\partial \tilde{u}_i / \partial x_i)$, the resolved viscous dissipation $\epsilon_\nu = \bar{\tau}_{ij} \tilde{S}_{ij}$, and the SGS dissipation $\epsilon_{SGS} = \mathcal{T}_{ij} \tilde{S}_{ij}$, where $\mathcal{T}_{ij} = \bar{\rho} \widetilde{u_i u_j} - \bar{\rho} \tilde{u}_i \tilde{u}_j$. For this work, the budget term of
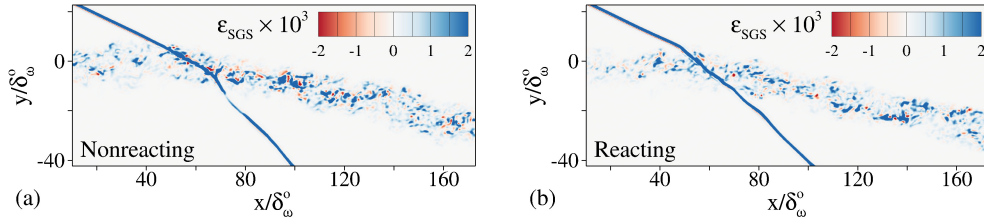
Figure 5: Instantaneous normalized SGS dissipation for (a) the nonreacting and (b) reacting shocked shear layer using a filter width of $8h$. Areas of backscatter (negative ϵ_{SGS}) are in red.

interest is ϵ_{SGS} which is the SGS dissipation or the flux of TKE between the resolved and SGS scales. The ϵ_{SGS} can be decomposed into a forward or a backward flux contribution as $\epsilon_{SGS}^{+} = 0.5(\epsilon_{SGS} + |\epsilon_{SGS}|)$ for the forward contribution and $\epsilon_{SGS}^{-} = 0.5(\epsilon_{SGS} - |\epsilon_{SGS}|)$ for the backward contribution. The term backscatter refers to the quantity ϵ_{SGS}^{-}.

For the filtering operation, we chose to use the smoothness-increasing accuracy-conserving filter presented by Li *et al.* (2019), which is a combination of three first-order shifted B-spline basis functions (top hats), the weights for which are such that the first six moment closure conditions are satisfied. This formulation allows for a high-order filter with a relatively compact stencil and was chosen over a true spectrally sharp filter so as to avoid filtering across the shock wave. For these preliminary results, we chose to use a filter width based on the grid size with filter-to-grid ratios (FGRs) of FGR = 8 and FGR = 16.

Instantaneous realizations of ϵ_{SGS} at a FGR = 8 are shown for the SDML-NR-Shocked and SDML-R-Shocked datasets in Figure 5. For both cases, positive values of TKE dominate. Only small pockets of negative values, corresponding to backscatter, are visible. In general, the instantaneous magnitudes of ϵ_{SGS} increase across the shock for both cases, with approximately 20% more increase in the mean across the shock for the reacting case compared to the nonreacting case.

Figure 6 shows the averaged profiles of ϵ_{SGS} calculated at the two filter wavelengths selected. Averages were calculated in the same manner and at the same locations as was described in Section 3. All cases show net positive ϵ_{SGS}, indicating that the TKE flux is everywhere transferred from the resolved to the SGS scales in the mean sense. As is consistent with the occurrence of the negative instantaneous ϵ_{SGS} in Figure 5, the mean profile of backscatter is nonzero for all cases. At the FGR = 8 filter width, the peak mean magnitude in the backscatter term is approximately 29% of the maximum total SGS dissipation curve for the SDML-NR case and 34% for the SDML-R case. For both shocked cases, the peak mean backscatter is approximately 24% of the total SGS dissipation. Thus, the fraction of backscatter is somewhat larger for the reacting case compared to the nonreacting case; however, the peak mean magnitude of backscatter is larger for the nonreacting case by a factor of 1.7. Also, the fraction of backscatter decreases across the shock for both cases, with a larger change in fraction of backscatter for the reacting case. Note that these profiles are normalized by the local properties of the shear layer. Thus, while the normalized mean magnitudes decrease across the shock, the absolute values increase, as noted earlier.

At FGR = 16, the magnitude of mean ϵ_{SGS} increases modestly compared to the FGR = 8 cases, with a slightly larger increase for the nonreacting case. The fraction
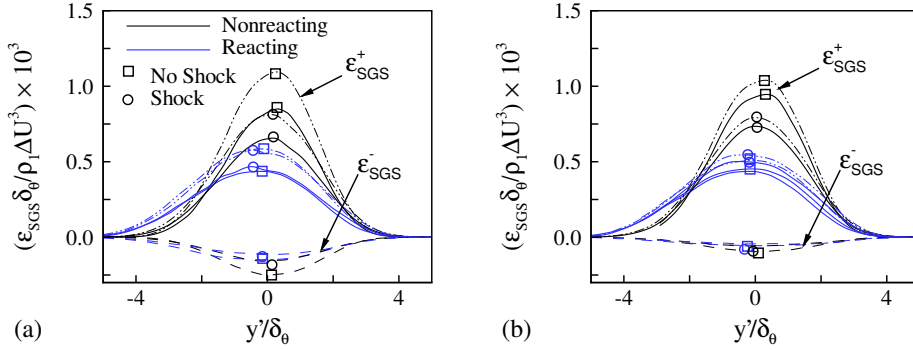
Figure 6: Mean profiles of SGS dissipation computed for a FGR of (a) 8 and (b) 16. Solid lines are the total value of ϵ_{SGS}, dash-dot-dot lines are the forward component ϵ_{SGS}^{+}, and the dashed lines are the backscatter component ϵ_{SGS}^{-}.

of mean backscatter decreases to 10% and 12% of the total SGS dissipation for the nonreacting and reacting cases for the larger FGR. The fraction of backscatter again decreases across the shock by similar amounts seen at the smaller FGR.

Note also that the comparison between the four conditions of reacting/nonreacting and shock/no shock is not a perfect comparison of filtered results. This is because the filter width was initially chosen on the basis of the grid size and applied to all four scenarios irrespective of the difference in the local momentum thickness and Reynolds number of each. Future work will incorporate closer matching of the filter properties with the local properties of the shear layers. A more thorough resolution study is also in order. The convergence study shown in Appendix A suggests that the resolution of the current simulations should be increased to ensure convergence of the filtered SGS backscatter.

5. Conclusions

This work investigates the nature of the cross-filter scale transfer of TKE in spatially developing, reacting and nonreacting, compressible shear layers interacting with an oblique shock. The goals of this paper are, first, to introduce the problem, second, to demonstrate the ability to adequately simulate the problem, and, third, to produce initial statistics of the magnitude of the TKE backscatter present in the flow. Results are consistent with the previous work of O'Brien *et al.* (2014a) in that the nondimensionalized average profiles of both forward- and backscatter are of similar magnitude and are lower for the reacting case than the nonreacting case. The current study found that the fraction of backscatter was larger for the reacting cases. The absolute value of backscatter increases across the shock, though nondimensionalizing the values by local flow quantities shows a slight decrease across the shock. Future work could explore the parameter space by varying the convective Mach number, the density ratio, the strength of the heat release rate, and the strength of the impinging shock. In addition, the influence of flow expansion on the shear layer could be investigated.
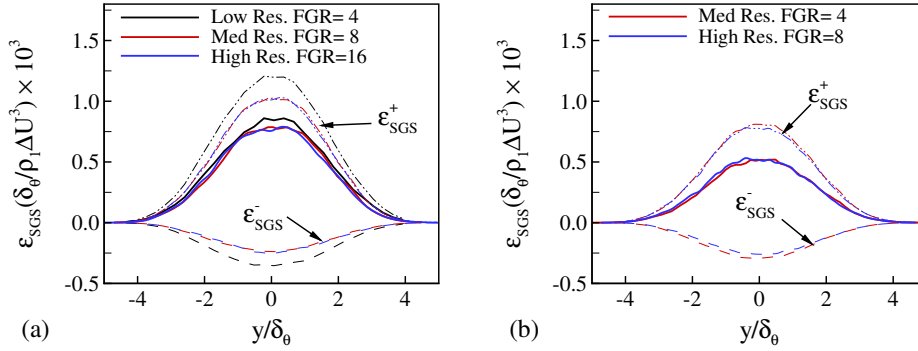
Figure 7: Convergence of the mean backscatter in the P&S $M_c = 0.7$ case. Results from two different filter sizes are shown, (a) FGR=8 and (b) FGR=4 based on the medium resolution grid. Solid lines are the total backscatter, dash-dot-dot lines are the forward scatter component, and dashed lines are the backscatter component.

Appendix A. Convergence of backscatter in Pantano & Sarkar (2002) case

A grid resolution study of the P&S test case in Section 2.1 was done in order to understand how the backscatter statistics converge with grid size. Figure 7 shows the backscatter calculation for the P&S case along with two additional simulations at half and twice the grid resolution. By applying a filter width of the same size across all resolutions, we found that the total SGS dissipation as well as the forward and back fluctuations is consistent for the medium- and high-resolution cases but deviates for the low-resolution case. The uniform grid spacings for the three resolutions of the P&S runs normalized by the momentum thickness are $h/\delta_\theta = 0.148$, 0.074, and 0.037. While the normalized resolutions are similar between the SDML cases discussed above and the medium grid P&S case, the P&S temporal shear layer statistics were taken at an instantaneous $Re_\theta = 1410$, which is significantly smaller than the Reynolds numbers for the SDML cases reported in Table 1. Therefore, the resolution of the SDML cases likely needs to be increased in future work to ensure convergence of the backscatter.

REFERENCES

GOTTLIEB, S. & SHU, C.-W. 1998 Total variation diminishing Runge-Kutta schemes. *Math. Comput.* **67**, 73–85.

HASSAN, E., PETERSON, D.M., WALTERS, K. & LUKE, E. 2016 Dynamic hybrid Reynolds-averaged Navier-Stokes/large-eddy simuaiton of a supersonic cavity. *J. Propul. Power*, **32**, 1343–1352.

HELM, C., PETERSON, D.M., LIM, J., PAGANINI, A. & LEE, T. 2025 Numerical and experimental investigation of a Mach 7 reactive flowpath. To be presented at the 2025 AIAA SciTech Forum.

KAZBEKOV, A. & STEINBERG, A.M. 2021 Physical space analysis of cross-scale turbulent kinetic energy transfer in premixed swirl flames. *Combust. Flame*, **229** 111403.

KAZBEKOV, A. & STEINBERG, A.M. 2022 Influence of flow structures and combustion on cross-scale turbulent kinetic energy transfer in premixed swirl flames. *P. Combust. Inst.* **39**, 2, 2329–2338.

KIM, J., BASSENNE, M., TOWERY, C.A.Z., HAMLINGTON, P.E., POLUDNENKO, A.Y. & URZAY, J. 2018 Spatially localized multi-scale energy transfer in turbulent premixed combustion. *J. Fluid Mech.* **848**, 78–116.

LI, X., RYAN, J.K., KIRBY, R.M. & VIUK, K. 2019 Smoothness-increasing accuracy-conserving (SIAC) filtering for discontinuous galerkin solutions over nonuniform meshes: superconvergence and optimal accuracy. *J. Sci. Comput.* **21**, 1150–1180.

LUO, Z., RICHARDSON, E.S., CHEN, J.H., LAW, C.K. & LU, T. 2012 Chemical explosive mode analysis for a turbulent ethylene jet flame in highly-heated coflow. *Combust. Flame*, **159**, 265–274.

MACCORMACK, R.W. & CANDLER, G.V. 1989 The solution of the Navier-Stokes equations using Gauss-Seidel line relaxation. *J. Comp. Fluids*, **17**, 135–150.

NOMPELIS, I., DRAYNA, T.W. & CANDLER, G.V. 2004 Development of a hybrid unstructured iImplicit solver for the simulation of reacting flows over complex geometries. *AIAA Paper* 2004-2227.

O'BRIEN, J., TOWERY, C.A.Z, HAMLINGTON, P.E., IHME, M., POLUDNENKO, A.Y. & URZAY, J. 2017 The cross-scale physical-space transfer of kinetic energy in turbulent premixed flame. P. Combust. Inst. **36**, 2, 1967–1975.

O'BRIEN, J., URZAY, J., IHME, M., MOIN, P. & SAGHAFIAN, A. 2014b Subrid-scale backscatter in reacting and inert supersonic hydrogen-air turbulent mixing layers. *J. Fluid Mech.* **743**, 554–584.

O'BRIEN, J., URZAY, J., POLUDNENKO, A.Y., HAMLINGTON, P.E. & IHME, M. 2014a Counter-gradient subgrid-scale transport and energy backscatter in turbulent deflagrations. *Annual Research Briefs*, Center for Turbulence Research, Stanford University, pp. 123–139.

PANTANO, C. & SARKAR, S. 2002 A study of compressibility effects in the high-speed turbulent shear layer using direct simulation. *J. Fluid Mech.* **451**, 329–371.

PIOMELLI, U., CABOT, W.H., MOIN, P. & LEE, S. 1991 Subgrid-scale backscatter in turbulent and transitional flows. *Phys. Fluids A-Fluid*, **3**, 1766–1771.

POPE, S.B. 2000 *Turbulent Flows.* Cambridge University Press.

RICHARDSON, L.F. 1922 *Weather Prediction by Numerical Process.* Cambridge University Press

SMAGORINSKY, J. 1963 General circulation experiments with the primitive equations. I: The basic experiment. *Mon. Weather Rev.* **9**, 3, 95–165.

SUBBAREDDY, P. & CANDLER, G.V. 2008 A fully discrete, kinetic energy consistent finite-volume scheme for compressible flow. *J. Comput. Phys.* **228**, 1347–1364.

TENNEKES, H. & LUMLEY, J.L. 1972 *A First Course in Turbulence.* MIT Press.

TOUBER, E. & SANDHAM, N.D. 2009 Large-eddy simulation of low-frequency unsteadiness in a turbulent shock-induced separation bubble. *Theor. Comp. Fluid Dyn.* **23**, 79–107.